ADVANCED MATERIALS
www.advmat.de

Revisiting the Impact of Anion Selection on Sulfur Redox Reaction Kinetics for High Sulfur Loading Lithium–Sulfur Batteries

Yue Fei, Matthew Li, Zhenfeng Li, Dichang Guan, Wenting Jia, Hao Zhang, Khalil Amine, and Ge Li**

Lithium bis(trifluoromethane)sulfonimide (LiTFSI) is widely used in lithium–sulfur (Li–S) battery electrolytes due to its stability with lithium polysulfides (LiPSs) and moderate compatibility with lithium metal anodes. However, LiTFSI presents environmental concerns due to its association with per- and polyfluoroalkyl substances (PFAS), which are environmentally persistent and potentially toxic, raises sustainability concerns. This research also reveals that LiTFSI limits sulfur redox reactions (SRRs), making it less effective than other lithium salts. Additionally, some salts previously considered incompatible with Li-S systems due to their reactivity with LiPSs are demonstrated to perform effectively. For the first time, a protective, porous cathode electrolyte interphase (CEI) formed in situ through reactions between salt anions and LiPS is reported. The cells delivered a high specific capacity of 1230.8 mAh g^{-1} at 0.05 C with a sulfur loading of ≈6 mg cm^{-2}, limited lithium anode, maintaining a capacity retention of 76.2% after 100 cycles at 0.1 C. Under harsh conditions, such as high sulfur loading, lean electrolyte conditions (3 µL mg^{-1}), and in anode-free cells, the cells continued to deliver outstanding capacity. This work provides valuable guidelines for understanding and selecting lithium salts to advance electrolyte design for Li–S batteries.

1. Introduction

Among all post-lithium-ion batteries, lithium–sulfur (Li–S) batteries stand out due to their high energy density and the abundant natural sulfur resource.[1] However, practical Li–S batteries are still under development due to challenges such as the "shuttle effect" and poor sulfur redox kinetics.[2] The former leads to poor cycle life, low Coulombic Efficiency (CE), and an unstable lithium metal anode, while the latter results in reduced energy density and necessitates an additional mass of catalyst and electrolyte.[3] These challenges hinder the advancement of practical Li–S batteries, particularly under harsh working conditions such as high sulfur loading, limited lithium metal anodes, and lean electrolyte systems.[3b,4]

Electrocatalytic cathode host materials,[5] separator modifications,[6] and electrolyte engineering,[7] are effective strategies for extending the life cycle and improving the energy density of Li–S batteries under harsh conditions. Among them, electrolyte engineering can not only regulate the sulfur cathode but also enhance the stability of the lithium metal anode.[8] In the Li–S system, electrolytes can be categorized into three groups. One can be called the "reducing LiPS solubility" group, which includes sparingly solvating electrolytes,[9] quasi-solid-state sulfur conversion electrolytes,[7b,10] encapsulating solvating electrolytes,[7a,11] carbonate-based CEI-forming (Cathode Electrolyte Interphase) electrolytes,[12] and solid electrolytes.[13] These electrolytes reduce the solubility of soluble lithium polysulfides (LiPSs)

Y. Fei, Z. Li, D. Guan, G. Li
Department of Mechanical Engineering
University of Alberta
Edmonton, Alberta T6G 1H9, Canada
E-mail: ge.li@ualberta.ca

M. Li, K. Amine
Chemical Sciences and Engineering Division
Argonne National Laboratory
9700 Cass Ave., Lemont, IL 60439, USA
E-mail: amine@anl.gov

D. Guan
School of Metallurgy and Environment
Central South University
Changsha, Hunan 410083, P. R. China

W. Jia, H. Zhang
Department of Chemical and Materials Engineering
University of Alberta
Edmonton, Alberta T6G 1H9, Canada

The ORCID identification number(s) for the author(s) of this article can be found under https://doi.org/10.1002/adma.202507459

DOI: 10.1002/adma.202507459

intermediates, thereby preventing the loss of active sulfur materials from the cathode and improving anode stability. The other category is strong solvating electrolytes, which enhance the solubility of LiPS to improve sulfur redox reaction (SRR) kinetics and sulfur utilization.[14] However, this approach usually requires additional protection for the lithium metal anode, as dissolved LiPS in the electrolyte can potentially corrode the anode. Last but not least, redox mediators and additives, which effectively improve SRR kinetics by decoupling the need for electronic transfer with physical contact between electrode and sulfur/lithium sulfide, enhance sulfur conversion and can significantly reduce the sulfur shuttle effect. These mediators have also been investigated to address the intrinsic issues of Li–S batteries.[15]

Some salts or compounds have been explored as additives or redox mediators to enhance the performance of both the sulfur cathode and the lithium metal anode. However, these additives and redox mediators are typically used at much lower concentrations (≈0.1 M) compared to the main salts in the electrolyte (≈1 M). Given the higher concentration of main salts, their impact on the SRR is likely to be more significant. Therefore, understanding and investigating the effects of these main electrolyte salts on SRR kinetics is critical, yet the understanding still needs to be improved. Recently, the competition between lithium bis(trifluoromethane)sulfonimide (LiTFSI) and lithium bis(fluorosulfonyl)imide (LiFSI) as the main salt in Li–S electrolytes has gained renewed attention. Initially, LiFSI was reported to be unsuitable for the Li–S system because it reacts to form an insulating $LiSO_x$ layer on the cathode surface, hindering the SRR.[16] However, recent studies have shown that LiFSI can reduce overpotentials in Li–S batteries, enable low-temperature operation, and improve cell life cycles.[17] Additionally, the presence of sulfate/sulfite-containing CEI layers has been reported with $LiNO_3$-containing electrolytes, suggesting that sulfur-containing CEI might actually benefit the sulfur cathode.[18] Thus, the $LiSO_x$ compounds formed by LiFSI might not be detrimental but beneficial to the cathode, effectively reducing the overpotential of the SRR. Other salts, such as lithium hexafluorophosphate ($LiPF_6$) and lithium tetrafluoroborate ($LiBF_4$), have been considered unsuitable for the Li–S system due to detrimental internal reactions.[4d,19] Despite these findings, the investigation into SRR kinetics and the role of different lithium salts in Li–S batteries remains limited and requires further exploration.[20] Moreover, growing concerns about the environmental impact of electrolytes containing fluorinated compounds like LiTFSI, which are associated with per- and polyfluoroalkyl substances (PFAS) that face regulatory restrictions due to their persistence and potential environmental hazards, make the need for suitable alternatives more urgent.[21] A systematic investigation of lithium salts is needed to identify safer, high-performance options for Li–S batteries.

This work systematically evaluates nine commercially available, commonly used lithium salts, comparing their effects on Li–S systems. The SRR kinetics, diffusion rates, and overpotentials are characterized and comprehensively analyzed. Interestingly, lithium bis(oxalato)borate (LiBOB), previously considered unsuitable for Li–S systems, was found to potentially be used in Li–S cells, delivering excellent performance even under harsh conditions. For the first time, a porous CEI derived from LiBOB has been identified. This CEI acts as a diffusion barrier for LiPS, effectively suppressing the shuttle effect. Unlike the CEI from carbonate-based electrolytes, the CEI allows solvent passage and enables solid–liquid–solid sulfur conversion. This ensures a higher discharge plateau (2.1–2.3 V) than solid-solid sulfur conversion (<1.9 V), enabling higher energy density and faster kinetics. The self-discharging behavior and lithium metal anode corrosion are successfully suppressed as well. For a sulfur loading of 6 mg cm^{-2} (10 mAh cm^{-2}) with ultra-thin Li foil (50 µm, 10 mAh cm^{-2}) as the anode, and an electrolyte-to-sulfur (E/S) ratio of 6 µL mg^{-1}, the cell delivers an excellent capacity of 1230.8 mAh g^{-1} at 0.05C, with 76.2% capacity retention over 100 cycles at 0.1 C. The cells perform well under higher sulfur loading (>10 mg cm^{-2}), lean electrolyte conditions, and even in anode-free cells. This work opens new opportunities for identifying better main salts for Li–S battery electrolytes, inspires further research on salt selection and design for Li–S batteries under harsh conditions, and highlights the potential of PFAS-free electrolytes in Li–S batteries.

2. Results and Discussion

2.1. Effects of Salt Anions on Sulfur Redox Reaction

To evaluate the effect of different salts on Li–S batteries, a Li_2S_6 solution is first prepared using Li_2S and sulfur powders in a stoichiometric ratio of 1:5. The solution, containing 50 mM Li_2S_6 in 1,2-Dimethoxyethane (DME)/1,3-Dioxolane (DOL) (1:1 vol ratio), remains a dark orange-brown color, referred to as the blank solution. Subsequently, 0.2 M of various lithium salts, including LiTFSI, lithium trifluoromethanesulfonate (LiOTf), lithium perchlorate ($LiClO_4$), $LiPF_6$, $LiNO_3$, LiFSI, lithium difluoro(oxalato)borate (LiDFOB), LiBOB, and $LiBF_4$, are added to the solution, as shown in **Figure 1a**. These salts can be categorized into two main groups upon complete dissolution and resting (3 days). The first group, which includes LiTFSI, LiOTf, $LiClO_4$, $LiPF_6$, and $LiNO_3$, does not exhibit a significant color change upon interaction with LiPS and is classified as the "non-reacting" group. The second group, referred to as the "reacting" group, consists of LiDFOB, LiBOB, and $LiBF_4$. These salts react with Li_2S_6, leading to observable color change and precipitation. LiFSI occupies a unique intermediate position, as it shows some precipitation in solution while retaining a brown color, indicating a partial but very slow reaction with Li_2S_6.[16]

Cyclic voltammetry (CV) was performed on symmetrical cells, using ethylene black electrodes with identical loadings, and a 0.2 M Li_2S_6 solution combined with 0.5 M of different lithium salts as the electrolyte. Two symmetrical peaks can be seen in the cathodic and anodic scans, indicating the oxidation and reduction reactions, respectively (Figure 1b). To delve deeper into the differences among the salts, the overpotential, peak current, and capacity of the different cells are calculated (Figure 1c; Figures S1–S6, Supporting Information).

The closer peak potentials suggest a more reversible redox reaction with lower overpotential, indicative of faster reaction kinetics. This trend follows the order of LiFSI, LiTFSI, $LiPF_6$, $LiClO_4$, LiOTf, and $LiNO_3$, from low to high. These findings align with previous reports that LiFSI results in a lower overpotential than LiTFSI.[17b,c] This suggests that the LiPS species are more easily

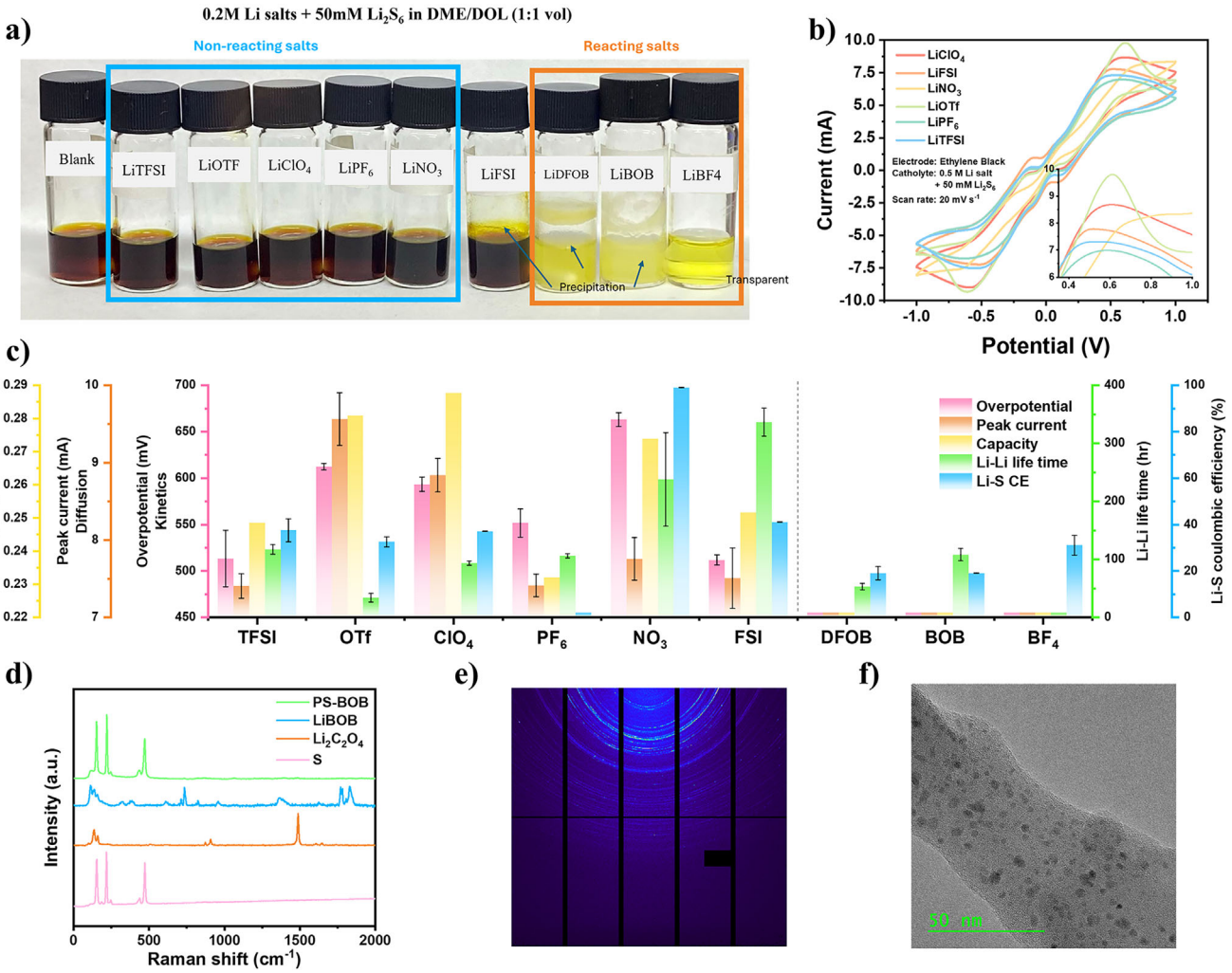

Figure 1. a) Visualization of the reaction of LiPS and different Li-salts, b) CV curves of S–S symmetrical cells with different Li salts. (Inset: Magnified view of CV curves), c) list of Li-salt anions and corresponding HOMO/LUMO (top) and electrochemical performance (bottom); d) Raman spectrum of the reaction product of LiPS and LiBOB (PS-BOB), LiBOB, $Li_2C_2O_4$ and S powder; e) GIXRD of the reaction product of LiPS and LiBOB; f) TEM image of the reaction product of LIPS and LiBOB.

interconverted between redox states, which is beneficial for improving the cycle life of the cell. However, $LiNO_3$, a commonly used electrolyte additive, exhibits the highest overpotential, likely due to its low degree of dissociation and the resulting low ionic conductivity of the electrolyte (Figure S5, Supporting Information). Regarding peak current, the salts rank from high to low: LiOTf, $LiClO_4$, $LiNO_3$, LiFSI, $LiPF_6$, and LiTFSI. According to the Randle Scevik equation,[22] under the same concentration, scan rate, and electrode area, the peak current reflects the diffusion rate, with a higher current response indicating better diffusion (see further discussion in Note S1, Supporting Information). The more significant current response observed with LiOTf may be due to changes in the solvation environment of the LiPS species, caused by the presence of different salts. These changes may lead to the formation of reversibly precipitated sulfur species, which in turn facilitate faster diffusion of Li ions and more efficient deposition of Li_2S on the cathode, and improving Li-ion diffusion within the cathode.[23] Conversely, LiTFSI exhibits the lowest current response, indicating slower ion diffusion in the LiTFSI system. Previous experiments have shown that reducing the concentration of LiTFSI improves discharge capacity, rate performance, and low-temperature performance.[17a,24] This improvement suggests that LiTFSI interacts with LiPS in the electrolyte, altering the solvation structure of Li^+. Specifically, when the concentration of $TFSI^-$ is reduced, LiPS tends to form aggregated structures, with polysulfides dominating the Li^+ solvation sheath instead of $TFSI^-$. This solvation structure enhances the SRR kinetics. Furthermore, the modification of the Li^+ solvation sheath can influence ionic conductivity and the composition of the SEI, which in turn also impacts SRR kinetics. Finally, integrating the area under the curve reveals the capacity, which follows the order: $LiClO_4$, LiOTf, $LiNO_3$, LiFSI, LiTFSI, and $LiPF_6$, from high to low. Capacity reflects the amount of sulfur that can react within the voltage window, with higher capacity indicating complete utilization of the active material and higher energy output during charge/discharge. $LiClO_4$ leads with the highest

capacity, followed by LiOTf and $LiNO_3$, while LiTFSI lags, highlighting its limitations for Li–S batteries, particularly under harsh conditions. To further verify the conclusions, Li–S cells with a sulfur loading of 5 mg cm^{-2} are tested, and the galvanostatic charge discharge (GCD) curves are shown in Figure S7 (Supporting Information). The results perfectly match the conclusions (See further discussion in Note S2, Supporting Information).

Besides the SRR, anode stability in Li–S batteries is another significant concern. To compare the anode stability of different systems, Li–Li symmetric cells were tested using different electrolytes (Figure S8, Note S3, Supporting Information). For the "non-reacting" group, 50 mM Li_2S_6 and 0.5 M salts (to keep consistency, limited by the solubility of $LiNO_3$) were used in the cell, as LiPS dissolution in the electrolyte significantly influences anode stability in Li–S cell. For the "reacting" group, only 0.5 M salts were used since LiPS reacts immediately upon addition. In the "non-reacting" group, the Li–Li lifetime follows the order: LiFSI, $LiNO_3$, LiTFSI, $LiClO_4$, $LiPF_6$, and LiOTf, from high to low. This ranking reflects the varying degrees of stability different salts provide in the electrolyte. For the "reacting" group, $LiBF_4$ failed in the Li–Li symmetrical test, indicating its unsuitability for the system. LiDFOB and LiBOB work for the system, but LiDFOB has only half the lifetime (50–60 h) compared to LiBOB (≈120 h), probably due to the lower LUMO of BOB^- and could be easier to be reduced on the lithium metal forming a desirable SEI.[25] For the coulombic efficiency of the Li||S cells, only $LiNO_3$ could reach a relatively higher CE of over 99%, while other salts fall behind with a CE lower than 40% (Figure S9, Supporting Information). This is consistent with previous research and why $LiNO_3$ is selected as an additive in most Li–S electrolyte systems.[26]

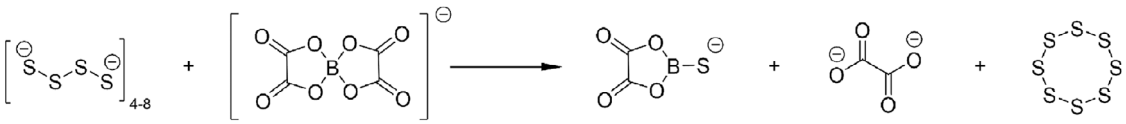

(1)

2.2. Mechanism Investigation of the Reaction of LiBOB and LiPS

To further study the composition of the precipitates formed from the reaction between LiPS and LiBOB, the solids are collected and dried for further analysis. Raman spectroscopy was first implemented for the reaction product (PS-BOB). Three characteristic peaks of elemental sulfur ≈150, 220, and 470 cm^{-1} have been observed, indicating the formation of elemental sulfur in the reaction (Figure 1d). Synchrotron-based Grazing Incidence X-ray Diffraction (GIXRD) was utilized to analyze the precipitation products. Unlike conventional XRD, which showed no distinct peaks (Figures S10 and S11, Supporting Information), the surface-sensitive nature and higher signal-to-noise ratio of GIXRD enabled the detection of a polycrystalline structure. This difference likely arises from the formation of small sulfur crystals near the surface (Figure 1e), which are more readily detected by GIXRD. The reaction between LiPS and LiBOB can be expected as Equation (1). A Transmission Electron Microscopy (TEM) image was further captured to analyze the reaction product of LiBOB and LiPS. The TEM images reveal a product with a non-crystalline bulk structure, likely representing the organic portion of the reaction. Additionally, the darker regions indicate a more crystalline structure, suggesting the presence of crystalline sulfur nanoparticles. In the presence of excess LiPS in the electrolyte, these sulfur nanoparticles could potentially undergo a disproportionation reaction with shorter-chain LiPS, forming soluble long-chain LiPS that dissolve into the electrolyte. This process contributes to the formation of a porous CEI structure on the cathode surface (See further discussion in Note S4, Figures S12–S14, Supporting Information).

2.3. Design of Fluorine-Free Electrolyte

After systematically evaluating various lithium salts, we propose a novel electrolyte design for high-loading Li–S batteries. While LiTFSI exhibits moderate anode stability, it underperforms in facilitating SRRs. We eliminated LiTFSI from the electrolyte to address these limitations, creating a fluorine-free solution comprising only $LiNO_3$ and LiBOB. In this design, $LiNO_3$ acts as the primary lithium carrier and SEI-forming agent, playing a crucial role in suppressing the polysulfide shuttle effect and maintaining high coulombic efficiency.[27] LiBOB was introduced due to its ability to react with LiPS and form a protective layer on the cathode, thereby improving cathode stability. LiBOB was chosen from several options in the "reacting" group of salts, as it reacts fast enough with LiPS to form the CEI and provides a relatively longer Li–Li lifetime, while LiFSI is unsuitable due to its slow reaction with LiPS, which leads to a gradual formation of the CEI layer on the cathode (See detailed discussion on salt selection in Note S5, Supporting Information). Together, these two salts create a multi-functional electrolyte consisting of 0.75 M $LiNO_3$ and 0.25 M LiBOB (≈5 wt.% for both, denoted as 5NB) in a DME/DOL (1:1 mol ratio) solvent mixture (Figures S15–S18, Supporting Information). This formulation is designed to improve both anode stability and overall cell performance, particularly in high-loading Li–S battery applications.

Notably, 0.75 M $LiNO_3$ is insoluble in the DME/DOL solvent, as shown in **Figure 2a**. However, similar to LiOTf,[28] the addition of 0.25 M LiBOB results in the dissolution of $LiNO_3$, rendering the electrolyte transparent. Nuclear magnetic resonance (NMR) spectroscopy reveals a downfield shift in the ^7Li signal upon the addition of $LiNO_3$ to the LiBOB solution, suggesting that NO_3^- enhances the electron cloud density around Li^+ solvated by

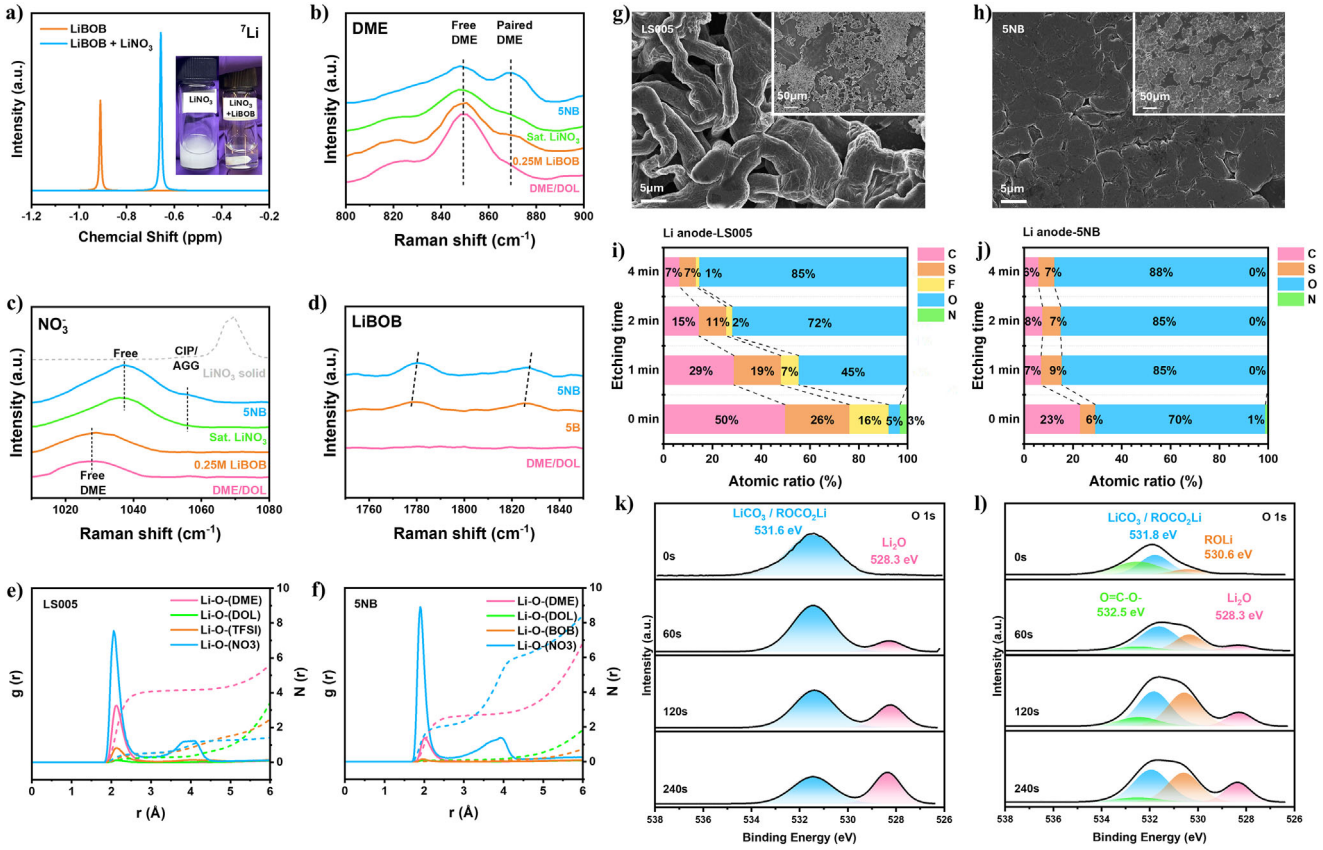

Figure 2. a) ^{7}Li NMR spectrum of 0.25 M LiBOB and 0.25 M LiBOB + 0.25 M $LiNO_3$ in DME/DOL, inserted images are the $LiNO_3$ solution in DME/DOL before and after adding LiBOB; b–d) Raman spectrum of different electrolytes and solvents; e) Calculated radial distribution functions g(r) and cumulative numbers N(r) for lithium ion in LS005 electrolyte and f) 5NB electrolyte; g) SEM images of cycled lithium metal in LS005 electrolyte and h) in 5NB electrolyte; i) Atomic percentage of elements during etching of lithium metal anode in LS005 electrolyte and j) in 5NB electrolyte; k) O 1s spectrum from in-depth XPS of lithium metal with LS005 electrolyte and l) with 5NB electrolyte.

BOB^-, indicating an interaction between NO_3^- and BOB^- (Figures S19 and S20, Supporting Information).[27] Raman spectroscopy reveals an increased proportion of paired DME when LiBOB and $LiNO_3$ are added to the solvent (Figure 2b–d; Figures S22 and S23, Supporting Information), suggesting a stronger Li-DME interaction. However, a saturated $LiNO_3$ solution does not exhibit a similar increase in paired DME, indicating a weak interaction between NO_3^- and DME (Figure 2b). In the Raman shift range of 1000–1080 cm^{-1}, NO_3^- vibrations are detected, with a peak at ≈1055 cm^{-1} corresponding to contact ion pairs (CIP) and aggregates (AGG), and a peak at ≈1035 cm^{-1} associated with free NO_3^- ions in the electrolyte (Figure 2c). Notably, in the 5NB sample (0.75 M $LiNO_3$ + 0.25 M LiBOB in DME/DOL), the CIP/AGG peak is significantly more intense than in the saturated $LiNO_3$ solution, suggesting that LiBOB stabilizes NO_3^- CIPs and AGGs, thereby enabling the dissolution of $LiNO_3$. Simultaneously, the paired-DME peak also strengthens, indicating that more DME molecules are coordinated in the presence of LiBOB. This special coordination likely contributes to the stabilization of NO_3^- CIPs and AGGs in the electrolyte. By analyzing both the NMR and Raman spectra, it can be concluded that Li-NO_3^- interactions are enhanced with LiBOB, making NO_3^- CIPs and AGGs more stable. This stabilization renders the solution transparent at a $LiNO_3$ concentration of 0.75 M, potentially explaining the improved dissolution of $LiNO_3$ in the presence of LiBOB.

The coordination of Li^+ was further examined through molecular dynamics (MD) simulations (Figure 2e,f; Figure S21, Supporting Information). The cumulative numbers N(r) indicate that DME predominantly occupies the first solvation shell of Li^+ in the LS005 (1 M LiTFSI + 0.2 M $LiNO_3$ in DME/DOL 1:1 vol) electrolyte. Conversely, in the 5NB system, $LiNO_3$ plays a significant role in modifying the first solvation shell of Li^+. This alteration promotes the formation of an anion-derived SEI layer on the lithium metal anode, thereby enhancing anode stability. SEM images were captured after cycling to compare the performance of different electrolytes on the lithium metal anode. Lithium dendrites are visible in the enlarged image (Figure 2g), indicating poor reversibility in lithium stripping and deposition in the LS005 electrolyte. The inserted lower magnification SEM image shows some areas of uniform deposition, but many dendrites remain (Figures S24–S29, Supporting Information). This corresponds with Figure 1c, where LiTFSI performs moderately in the Li–Li symmetric system. In contrast, the higher magnification SEM image of the 5NB system shows large lithium chunks and uniform deposition without dendrites, indicating better reversibility and enabling Li–S cells to operate under

harsh conditions, such as low N/P ratios and in anode-free cells.

To further investigate the SEI components on the lithium metal anode, in-depth XPS analysis was conducted on the cycled anodes for both LS005 and 5NB electrolytes. Atomic percentages of each SEI element at different etching times are shown in Figure 2i,j for LS005 and 5NB electrolytes, respectively. In the LS005 system, the carbon content decreases with increased etching time, along with sulfur, fluorine, and nitrogen. At the same time, oxygen begins to dominate in the inner layer, indicating a typical organic-rich outer layer and the inorganic-rich inner layer (Li_2O, Li_3N, LiF, and Li_2S) (Figure S30, Supporting Information).

Similarly, the 5NB system shows a carbon-richer outer layer, though with significantly lower carbon content (23% vs 50% in LS005), and an oxygen-dominant inner layer (>85% after 1 min of etching). The C 1s spectrum of 5NB reveals new peaks for R—O—C═O and C_2O_4, likely due to LiBOB salts in the electrolyte, known to form a soft organic SEI with compounds like $ROCO_2$-Li and O═C—O.[29] The presence of a large amount of $LiNO_3$ contributes to the formation of oxygen-rich components such as Li_2O and $Li_2S_2O_3$ (Figure S31, Supporting Information), aligning with these findings.

In the high-resolution O 1s spectrum (Figure 2k,l), only Li_2O and $ROCO_2$-Li are detected in the LS005 system, while the 5NB system contains additional oxygen-containing compounds like RO-Li, $ROCO_2$-Li, and O═C—O. As etching progresses, O═C—O decreases while Li_2O increases, with RO-Li and $ROCO_2$-Li remaining dominant. This oxygen-rich SEI, likely formed from the decomposition of LiBOB, $LiNO_3$, and ether solvents such as DOL, contributes to improved lithium deposition and reversibility, as supported by previous studies.[30] This explains the differences in lithium morphology observed in the SEM images between the electrolytes. These findings are consistent with Li RDF simulations, which suggest that a NO_3^- -rich coordination structure may lead to an oxygen- and nitrogen-rich inner SEI layer. This SEI plays a crucial role in protecting the lithium anode from corrosion by polysulfides in the electrolyte. The S 2p spectrum shows sulfur content of 7–26% on lithium metal in the LS005 system, with Li_2S and Li_2S_2 as predominant species, primarily from dissolved LiPS from the cathode. In contrast, the 5NB system shows much lower sulfur content (6–9%), suggesting less LiPS dissolution. The underlying mechanism behind this observation will be discussed in detail in the following section.

2.4. Electrochemical Measurements and Cell Performance

To compare the cycling performance of different electrolytes, Li||S cells are evaluated at a 1 C rate. LiDFOB is tested for comparison, as it serves a similar function to LiBOB, as discussed previously. However, it exhibits a lower capacity and faster decay rate than LiBOB (**Figure 3a**). To compare with a commonly used baseline electrolyte, high-loading sulfur cathodes (>5 mg cm^{-2}) and a lean electrolyte condition (5 µL mg^{-1}) were employed. Under these testing conditions, the 5NB electrolyte delivered a high initial specific capacity of 1136 mAh g^{-1}, surpassing the 993 mAh g^{-1} capacity observed for the LS005 electrolyte at 0.05 C (Figure 3b). At higher current densities of 0.1 C, the cell with the 5NB electrolyte maintained an excellent reversible capacity of over 900 mAh g^{-1}. In contrast, due to sluggish kinetics under the lean electrolyte system, the cell with the LS005 electrolyte delivered only ≈200 mAh g^{-1}. Examination of the GCD curves reveals that both cells exhibit a typical two-plateau discharge curve during the first cycle, indicative of the solid–liquid–solid conversion of sulfur (Figure 3c; Figures S32 and S33, Supporting Information).[4a] However, for the LS005 system, the second discharge plateau vanishes when the current density is increased to 0.1 C. This plateau corresponds to the liquid–solid conversion, hindered by slow kinetics. The presence of LiTFSI inhibits the SRR, hindering the effective deposition of Li_2S.

High-loading sulfur cathodes, lean electrolytes, and low N/P ratios (collectively referred to as harsh conditions) are crucial for practical applications. To assess the feasibility of 5NB electrolytes under such conditions, high-loading sulfur cathodes were prepared and tested (Figure 3d; Figure S34, Supporting Information). With high sulfur loading (>5 mg cm^{-2}), lean electrolyte conditions (6 µL mg^{-1}), and a low N/P ratio (50 µm, 10 mAh cm^{-2} lithium foil), the cell delivered an excellent capacity of 1231 mAh g^{-1} at 0.05 C, with a capacity retention of 80% over 95 cycles at 0.1 C, demonstrating the perfect reversibility. In contrast, the LS005 system initially delivered 1062.6 mAh g^{-1} with similar capacity during early cycles but experienced gradual capacity fade, failing after 63 cycles. The coulombic efficiency dropped to 76.5%, while the 5NB system maintained a CE of 97.82% even after 120 cycles, highlighting a significant reduction in the shuttle effect in the 5NB system. At higher sulfur loadings (>10 mg cm^{-2}), the 5NB system still delivered 1034 mAh g^{-1}, achieving over 6.8 mAh cm^{-2} after 70 cycles with 80.5% capacity retention at 0.1 C (Figure 3f; Figures S35 and S36, Supporting Information), and an average CE above 98.5%.

Limited lithium metal anodes can enhance energy density further, while anode-free cells with lithiated cathodes and current collectors as the anode could achieve the highest energy density. In this context, Li_2S||Ti anode-free Li–S batteries were tested to investigate the feasibility of the 5NB electrolyte under extreme working conditions. As shown in Figure 3e, the anode-free cell exhibited a high initial charging capacity of 1168.8 mAh g^{-1} (Figure S37, Supporting Information) and maintained capacity retention of 50% after 64 cycles at 0.1 C, indicating the feasibility of the 5NB electrolyte under extreme conditions. A Li–S pouch cell was also assembled using a sulfur loading of 4 mg cm^{-2} for the cathode and 50 µm lithium foil as the anode, with an E/S ratio of 3 µL mg^{-1} (Figure 3g). The cell delivered a specific capacity of 1020.9 mAh g^{-1}, demonstrating the potential of 5NB electrolyte for commercial cells and energy storage applications.

2.5. Improve in Suppressing Self-Discharging Behavior

In addition to excellent cycling performance, other issues of Li–S batteries are also investigated with the 5NB system. Due to sulfur dissolution and anode reaction, Li–S batteries undergo severe self-discharging, even at rest. A visual experiment is conducted to compare Li anode corrosion in two systems. Sulfur powder is placed in a glass vial with electrolytes and then sink to the bottom. A piece of lithium foil is then placed in the solution, floating on top due to its low density. This setup forms a lithium-electrolyte-sulfur configuration, same as the configuration in the

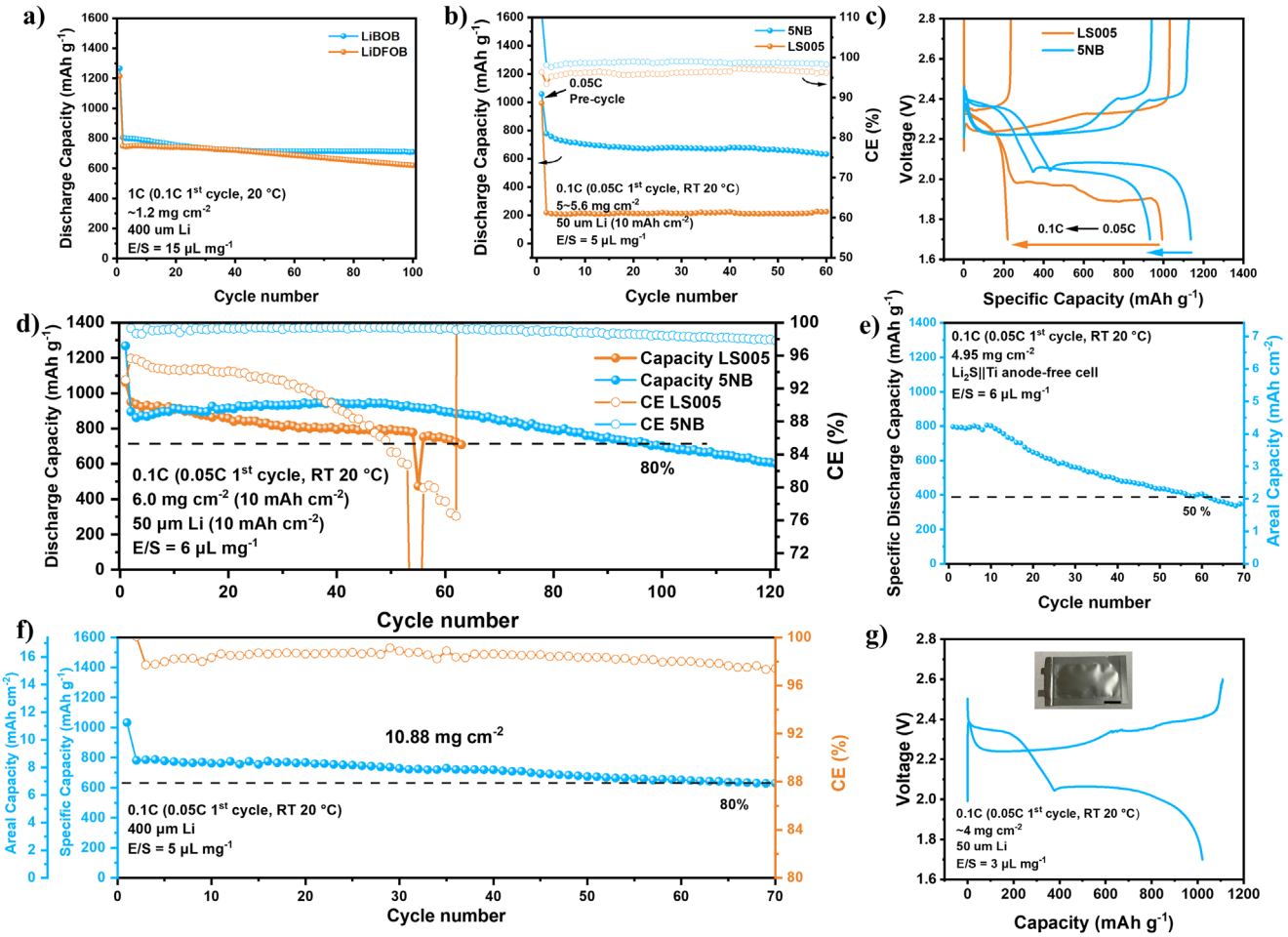

Figure 3. a) Comparison of the cycling performance of electrolyte containing LiBOB and LiDFOB, b) comparison of the cycling performance of LS005 and 5NB electrolyte under high sulfur loading and lean electrolyte condition, and c) corresponding GCD curves; d) Cycling performance of Li–S cell with 5NB electrolyte under harsh conditions; e) cycling performance of anode-free Li_2S||Ti cells; f) Cycling performance of Li–S cell with ultrahigh sulfur loading (>10 mg cm^{-2}), and g) Li–S pouch cell with 5NB electrolyte, with a lean electrolyte condition of 3 µL mg^{-1}, scale bar: 1 cm.

battery. After resting for 30 days, the vial with LS005 electrolyte showed a noticeable color change, indicating the dissolution of LiPS and reactions between the components (Figures 4a, S38, Note S6, Supporting Information). In contrast, the vial with 5NB electrolyte remained clear, demonstrating its effectiveness in preventing sulfur dissolution and protecting the lithium metal anode. For comparison, a glass vial with LS005 electrolyte without lithium foil was also set for 30 days, showing no significant color change. This indicates that the color change is related to the reaction of dissolved sulfur with the lithium foil. Furthermore, a pure DME/DOL solvent was tested under the same conditions. After 7 days, the vial containing only the solvent exhibited a more pronounced color change, indicating that the salts significantly influence sulfur dissolution and the reaction with lithium. Therefore, salt selection is crucial for the Li–S systems, especially under harsh conditions and longer cycling life.

The self-discharging behavior in different electrolytes is further tested. The cells are first cycled for 10 cycles at 0.5 C and then rested for 1, 3, and 7 days, respectively. After resting, the cell with the 5NB electrolyte shows a diminished capacity drop, with capacity retention of more than 90% even after 7 days of resting (Figure 4b–g). In contrast, severe self-discharge is observed in the LS005 electrolyte. After one day of rest, the cell lost 20% of its capacity (80% capacity retention), and retention dropped to 56% and 52% after 3 and 7 days, respectively. The first discharge plateau disappears from the GCD curves, indicating that long-chain LiPS are reduced to short-chain LiPS due the shuttle effect and the self-discharging behavior. This result confirms that the 5NB electrolyte is suitable for long-term storage and cycling, as it effectively mitigates the self-discharge issue compared to LS005.

2.6. Mechanism Investigation of How the Electrolyte Improve the Cell Performance

After comparing the electrochemical performance of the 5NB electrolyte, the mechanisms behind its improved performance in Li–S batteries are investigated. In-situ Raman spectroscopy and operando XRD are conducted on each cell (Figure 5a–c; Figures S39 and S40, Supporting Information). The LiPS signal is detected ≈490 cm^{-1} Raman shift. In the LS005 electrolyte, Li_2S_4 is first detected, indicating the dissolution of LiPS into the

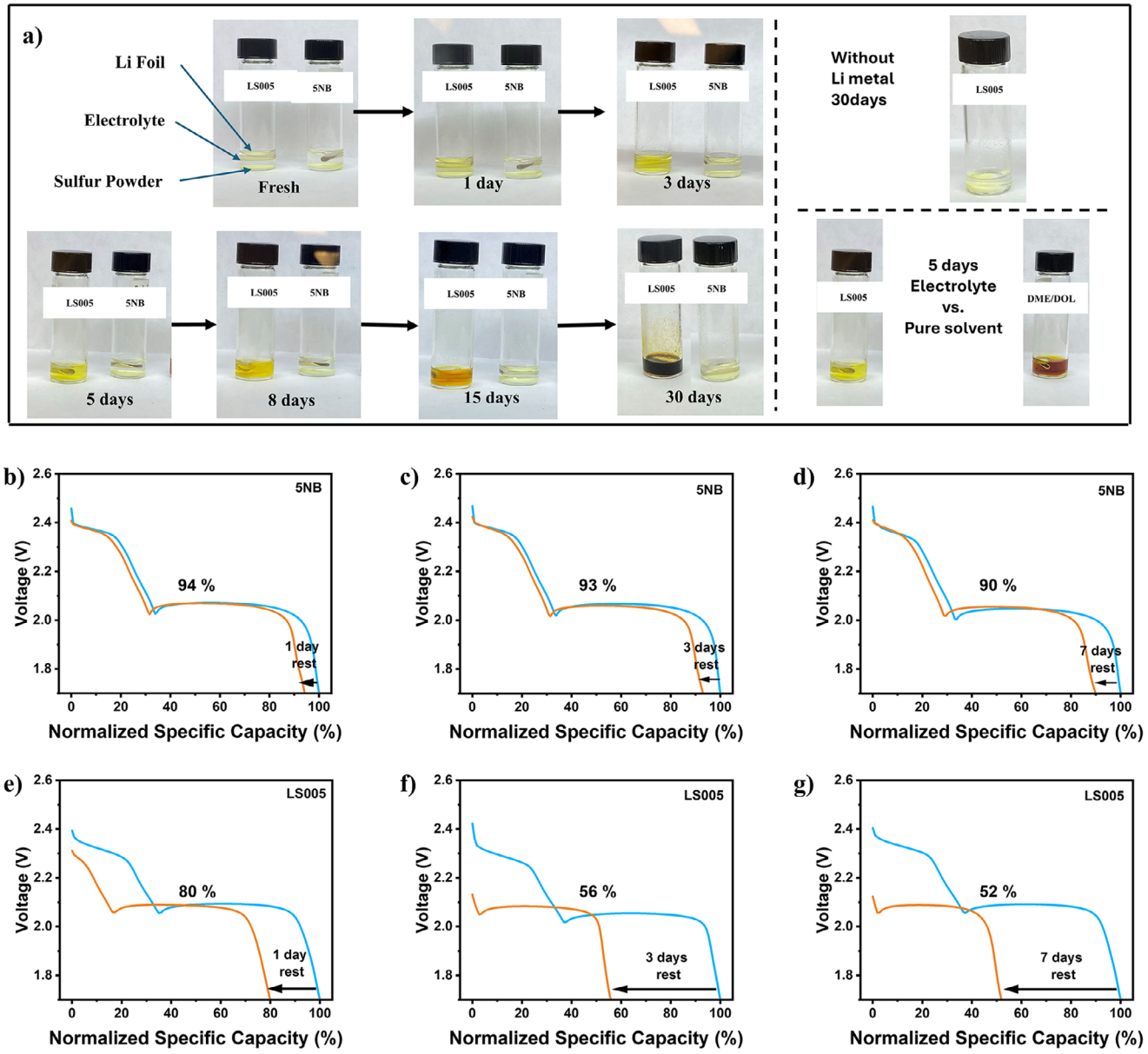

Figure 4. a) Visualization test of sulfur dissolution and lithium metal anode corrosion after 1, 3, 5, 8, 15, and 30 days, with control samples (no lithium foil) and with pure solvents; b–g) self-discharging test of Li–S with b–d) 5NB electrolyte and e–g) LS005 electrolyte, after 1, 3, and 7 days, respectively.

electrolyte. This signal diminishes as the discharge proceeds but reappears during the charging process, remaining present at the end of the charging cycle. This indicates the incomplete conversion of LiPS. In comparison, the LiPS signal in the 5NB electrolyte is only detected at the beginning of the charging process. It diminishes quickly, indicating the fast conversion of LiPS without LiTFSI. No LiPS signal is detected at the end of the charging process, demonstrating complete sulfur conversion and high sulfur utilization.

In the in-depth X-ray photoelectron spectroscopy (XPS) analysis, the atomic ratio of different elements is shown in Figure 5b–d (Figures S41 and S42, Supporting Information). The cathode with LS005 electrolyte primarily contains C and F, whereas the 5NB system predominantly contains C. In the 5NB system, the carbon content decreases as the etching time increases, indicating a carbon-rich outer layer. The carbon-containing compounds that could be the formation of the CEI by LiBOB, will be discussed in the next section. Additionally, the sulfur species on the surface of the cathode in the 5NB electrolyte remain low and increase after etching, indicating the presence of the CEI layer (Note S4, Supporting Information). The F content is mainly from the PVDF binder in the electrode.

The high-resolution S 2p and N 1s spectra are shown in Figure 5e–h. The LS005 system detects S_8, LiPS, and components such as thiosulfate and R-SO_2-R. S_8 and LiPS are generated by sulfur, while thiosulfate is likely generated by $TFSI^-$ anions, and R-SO_2-R is a part of the $TFSI^-$ anion. As discussed in Figure 1c, the presence of $TFSI^-$ anions in the cathode is not beneficial to

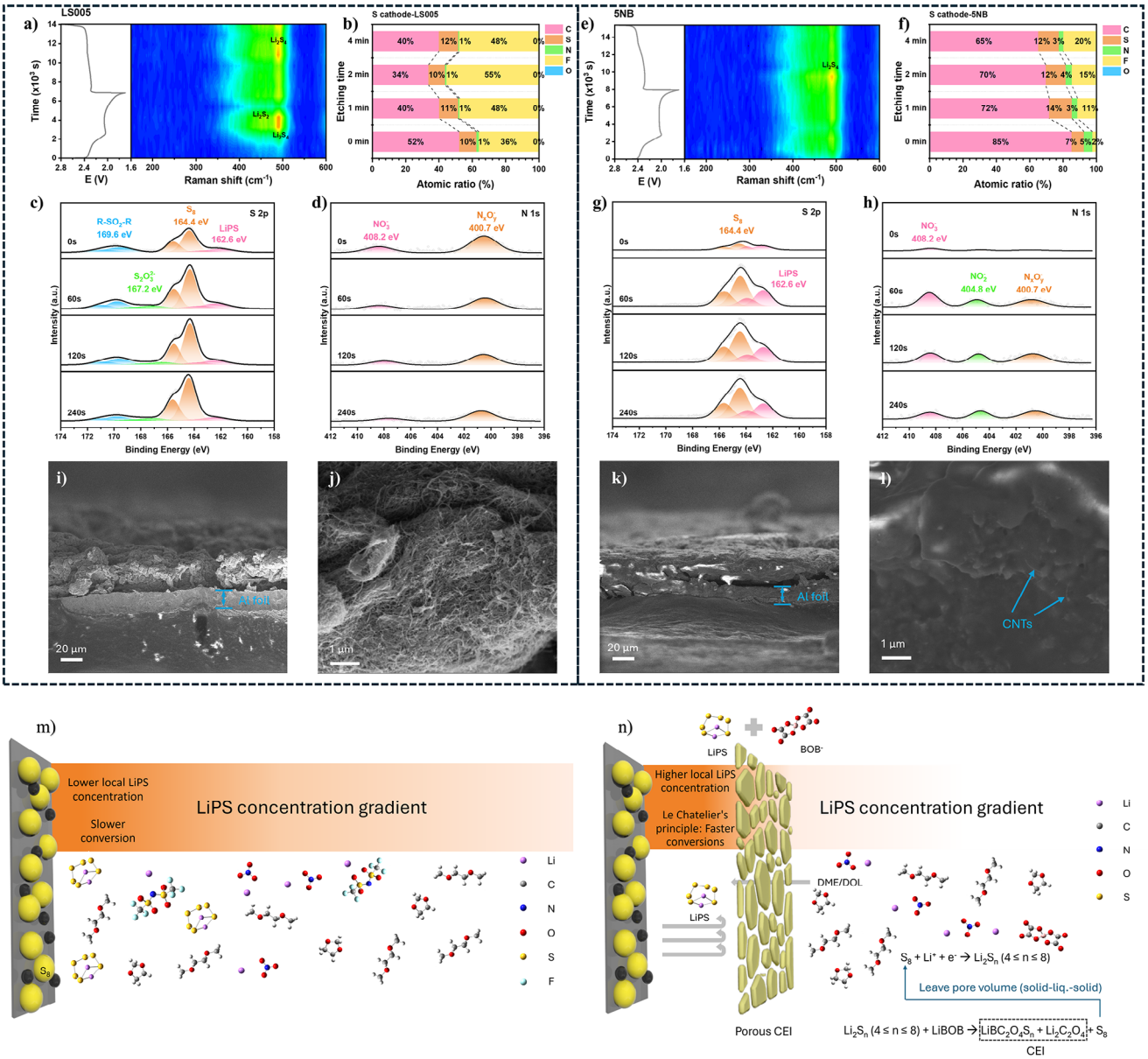

Figure 5. a) In situ Raman spectrum of Li–S cells with LS005 electrolyte, b) atomic ratio derived from in-depth XPS analysis, c) S 2p, and d) N 1s spectrum of sulfur cathodes cycled in LS005 electrolyte. e) In situ Raman spectrum of Li–S cells with 5NB electrolyte, f) atomic ratio derived from in-depth XPS analysis, g) S 2p and h) N 1s spectrum of sulfur cathodes cycled in 5NB electrolyte. i,j) cross-sectional SEM image for cycled S/CNT cathode in LS005 electrolyte and k,l) in 5NB electrolyte; o) schematic diagram of LS005 electrolyte system and n) 5NB electrolyte system.

the SRR. In comparison, the 5NB electrolyte only contains LiPS and S_8 in the S 2p spectrum, and the sulfur species on the surface are limited, indicating the presence of a CEI layer. Additionally, the N 1s spectrum reveals more nitrogen-containing species, possibly derived from the NO_3^- anion. Nitrates are considered beneficial for sulfur nucleation during the charging process,[26b] which might contribute to the excellent performance of the sulfur cathode in electrochemical tests.

To verify the presence of the CEI layer on the cathode, cross-sectional SEM images of the cycled cathode were captured (Figure 5i–l). In the LS005 system, the cycled cathode shows no significant changes compared to the fresh cathode (Figures S43 and S44, Supporting Information), and the CNT/S structure remains clearly visible. However, in the 5NB system, the surface morphology changes, with the CNT cathodes covered by a smooth layer, obscuring the stacked CNT network. At higher magnification (Figure 5i), some CNTs are still visible beneath the smooth layer, identified as the CEI layer formed by the reaction between LiPS and LiBOB. The intrinsic characteristics of the cycled S/CNT cathode with the 5NB electrolyte were further analyzed using FIB-SEM (Figure S45, Supporting Information). The stacked nanotube structure remained intact after cycling, indicating that the cathode structure was not disrupted and the carbon surface was not fully covered by the reaction products of LiPS

and LiBOB. This preserved surface allows for sufficient S/Li_2S growth, enabling the long-term cycling stability of the cell.

In the control sample, once LiPS forms during the SRR, they diffuse toward the lithium metal anode due to the concentration gradient, resulting in side reactions, low CE, and reduced specific capacity (Figure 5m). In contrast, in the 5NB system, dissolved LiPS reacts with LiBOB, forming a CEI layer on the cathode surface. As sulfur and LiPS undergo disproportionation and comproportionation reactions, elemental sulfur possibly re-dissolves, leaving behind a porous CEI structure (Figure 2f). This porous CEI acts as a diffusion barrier, slowing down the mass transfer of solvents and salts in the electrolyte. Meanwhile, polysulfide anions tend to form larger solvation structures due to their elongated S—S bonding network and their propensity to exist as ion pairs or aggregates in ether-based systems, driven by their divalent negative charge and strong Coulombic interactions with cations.[7a,31] The larger polysulfide solvation structure diffuses more slowly with the presence of the diffusion barrier, effectively suppressing the polysulfide shuttle effect. In contrast, solvated Li^+ ions and pure solvent molecules, due to their significantly smaller size, can still pass through (Figure 5n).

The presence of two distinct discharge plateaus further confirms that the porous CEI allows solvent interaction (Figure S46, Note S7, Supporting Information), maintaining a higher discharge voltage of 2.1–2.3 V, compared to the 1.9 V typically observed in solid-solid conversions. This elevated discharge voltage enhances energy density, and the solid-liquid-solid reaction enables faster kinetics than solid-solid reactions.[32] Additionally, the suppression of the LiPS shuttle is evidenced by improved capacity retention (Figure 3), visualization tests (**Figure 4**), and structural characterizations (**Figure 5**). By slowing down the diffusion of LiPS, the CEI not only facilitates faster SRR kinetics but also protects the lithium metal anode from LiPS-induced corrosion, thereby enhancing both stability and longevity.

3. Conclusion

In this study, we demonstrate that while the commonly used LiTFSI salt exhibits only good compatibility with LiPS, it lags in terms of SRR overpotential, diffusion rates, and kinetics when used as the main salt in the electrolyte. This has hindered the development of high-energy-density Li–S batteries over the past 20 years. Our findings reveal that salts not only affect the SRR but also influence LiPS dissolution and the self-discharging behavior in Li–S batteries. The cell performs excellently by eliminating LiTFSI and introducing new "LiPS reacting" salts into the electrolyte, previously considered unsuitable for the Li–S system. This fluorine-free electrolyte, composed of $LiNO_3$ and LiBOB in a conventional DME/DOL solvent, enables the formation of a porous CEI that acts as a diffusion barrier for LiPS, effectively suppressing the shuttle effect. As a result, Li||S cells achieve a specific capacity of 1230.8 mAh g^{-1} at 0.05 C and maintains a capacity retention of 76.2% after 100 cycles at a high sulfur loading of 6 mg cm^{-2} (10 mAh cm^{-2}) and a limited lithium anode (10 mAh cm^{-2}). Even under higher loading (>10 mg cm^{-2}), lean electrolyte conditions (3 µL mg^{-1}), and in anode-free cells, the cell continues to deliver outstanding capacity. This work opens new opportunities for identifying superior main salts for Li–S battery electrolytes beyond LiTFSI while addressing environmental concerns associated with PFAS in fluorinated salts. It also inspires further research into salt selection and design for Li–S batteries under challenging conditions, especially the sluggish SRR in thick electrodes with lean electrolyte, and even for solid-state Li–S batteries.

Supporting Information

Supporting Information is available from the Wiley Online Library or from the author.

Acknowledgements

This work was financially supported by the Natural Sciences and Engineering Research Council of Canada (NSERC) through the Discovery Grant Program (RGPIN-2020-05184). This work was also supported by funding from the Canada First Research Excellence Fund as part of the University of Alberta's Future Energy Systems research initiative.

Conflict of Interest

The authors declare no conflict of interest.

Data Availability Statement

The data that support the findings of this study are available from the corresponding author upon reasonable request.

Keywords

high loading batteries, lean electrolyte batteries, lithium–sulfur batteries, sulfur redox reaction

Received: April 19, 2025
Revised: June 2, 2025
Published online: July 10, 2025

[1] a) N. Jones, *Nature* **2024**, *636*, 248; b) Z. P. Cano, D. Banham, S. Ye, A. Hintennach, J. Lu, M. Fowler, Z. Chen, *Nat. Energy* **2018**, *3*, 279; c) M. Winter, B. Barnett, K. Xu, *Chem. Rev.* **2018**, *118*, 11433; d) M. Li, J. Lu, Z. Chen, K. Amine, *Adv. Mater.* **2018**, *30*, 1800561; e) G. Zhou, H. Chen, Y. Cui, *Nat. Energy* **2022**, *7*, 312; f) Q. Pang, X. Liang, C. Y. Kwok, L. F. Nazar, *Nat. Energy* **2016**, *1*, 16132; g) A. Bhargav, J. He, A. Gupta, A. Manthiram, *Joule* **2020**, *4*, 285; h) P. Xiao, X. Yun, Y. Chen, X. Guo, P. Gao, G. Zhou, C. Zheng, *Chem. Soc. Rev.* **2023**, *52*, 5255.

[2] a) L. Zhou, D. L. Danilov, F. Qiao, J. Wang, H. Li, R. A. Eichel, P. H. L. Notten, *Adv. Energy Mater.* **2022**, *12*, 2202094; b) J. Qin, R. Wang, P. Xiao, D. Wang, *Adv. Energy Mater.* **2023**, *13*, 2300611.

[3] a) Z.-X. Chen, M. Zhao, L.-P. Hou, X.-Q. Zhang, B.-Q. Li, J.-Q. Huang, *Adv. Mater.* **2022**, *34*, 2201555; b) M. Zhao, B.-Q. Li, H.-J. Peng, H. Yuan, J.-Y. Wei, J.-Q. Huang, *Angew. Chem., Int. Ed.* **2020**, *59*, 12636.

[4] a) Y. Fei, G. Li, *Adv. Funct. Mater.* **2024**, *34*, 2312550; b) J. Chen, Y. Fu, J. Guo, *Adv. Mater.* **2024**, *36*, 2401263; c) M. Wang, Z. Bai, T. Yang, C. Nie, X. Xu, Y. Wang, J. Yang, S. Dou, N. Wang, *Adv. Energy Mater.* **2022**, *12*, 2201585; d) S. S. Zhang, *J. Power Sources* **2013**, *231*, 153; e) A. Rosenman, E. Markevich, G. Salitra, D. Aurbach, A. Garsuch, F. F. Chesneau, *Adv. Energy Mater.* **2015**, *5*, 1500212; f) S. Zhang, K. Ueno, K. Dokko, M. Watanabe, *Adv. Energy Mater.* **2015**, *5*, 1500117.

[5] a) W. Hua, T. Shang, H. Li, Y. Sun, Y. Guo, J. Xia, C. Geng, Z. Hu, L. Peng, Z. Han, C. Zhang, W. Lv, Y. Wan, *Nat. Catal.* **2023**, *6*, 174; b) Z. Shen, X. Jin, J. Tian, M. Li, Y. Yuan, S. Zhang, S. Fang, X. Fan, W. Xu, H. Lu, J. Lu, H. Zhang, *Nat. Catal.* **2022**, *5*, 555; c) H. Li, R. Meng, C. Ye, A. Tadich, W. Hua, Q. Gu, B. Johannessen, X. Chen, K. Davey, S.-Z. Qiao, *Nat. Nanotechnol.* **2024**, *19*, 792; d) Y. Fei, Z. Li, P. Li, X. Zhang, Z. Xu, W. Deng, H. Zhang, G. Li, *ACS Appl. Mater. Interfaces* **2024**, *16*, 53833; e) Z. Wang, C. Wei, H. Jiang, Y. Zhang, K. Tian, Y. Li, X. Zhang, S. Xiong, C. Zhang, J. Feng, *Adv. Mater.* **2024**, *36*, 2306015; f) C. Wei, B. Xi, P. Wang, Y. Liang, Z. Wang, K. Tian, J. Feng, S. Xiong, *Adv. Mater.* **2023**, *35*, 2303780.

[6] a) Y. Zuo, X. Jiao, Z. Huang, J. Lei, M. Liu, L. Dong, W. Yan, J. Zhang, *Adv. Funct. Mater.* **2024**, *34*, 2405853; b) R. Zhou, Y. Ren, W. Li, M. Guo, Y. Wang, H. Chang, X. Zhao, W. Hu, G. Zhou, S. Gu, *Angew. Chem., Int. Ed.* **2024**, *63*, 202405417.

[7] a) X.-Q. Zhang, Q. Jin, Y.-L. Nan, L.-P. Hou, B.-Q. Li, X. Chen, Z.-H. Jin, X.-T. Zhang, J.-Q. Huang, Q. Zhang, *Angew. Chem., Int. Ed.* **2021**, *60*, 15503; b) Y. Liu, L. Xu, Y. Yu, M. He, H. Zhang, Y. Tang, F. Xiong, S. Gao, A. Li, J. Wang, S. Xu, D. Aurbach, R. Zou, Q. Pang, *Joule* **2023**, *7*, 2074.

[8] Y. S. Meng, V. Srinivasan, K. Xu, *Science* **2022**, *378*, abq3750.

[9] a) M. Cuisinier, P. E. Cabelguen, B. D. Adams, A. Garsuch, M. Balasubramanian, L. F. Nazar, *Energy Environ. Sci.* **2014**, *7*, 2697; b) C. Zhao, G. L. Xu, T. Zhao, K. Amine, *Angew. Chem., Int. Ed.* **2020**, *59*, 17634.

[10] Q. Pang, A. Shyamsunder, B. Narayanan, C. Y. Kwok, L. A. Curtiss, L. F. Nazar, *Nat. Energy* **2018**, *3*, 783.

[11] L.-L. Su, N. Yao, Z. Li, C.-X. Bi, Z.-X. Chen, X. Chen, B.-Q. Li, X.-Q. Zhang, J.-Q. Huang, *Angew. Chem., Int. Ed.* **2024**, *63*, 202318785.

[12] a) F. He, X. Wu, J. Qian, Y. Cao, H. Yang, X. Ai, D. Xia, *J. Mater. Chem. A* **2018**, *6*, 23396; b) M. He, X. Li, X. Yang, C. Wang, M. L. Zheng, R. Li, P. Zuo, G. Yin, X. Sun, *Adv. Energy Mater.* **2021**, *11*, 2101004.

[13] J. T. Kim, H. Su, Y. Zhong, C. Wang, H. Wu, D. Zhao, C. Wang, X. Sun, Y. Li, *Nat. Chem. Eng.* **2024**, *1*, 400.

[14] Y. Ren, A. Manthiram, *Adv. Energy Mater.* **2022**, *12*, 2202566.

[15] a) M. Zhao, X. Chen, X.-Y. Li, B.-Q. Li, J.-Q. Huang, *Adv. Mater.* **2021**, *33*, 2007298; b) X. Lv, Z. Qian, X. Zhang, X. Zhang, H. Zheng, M. Liu, Y. Liu, J. Lu, *Angew. Chem., Int. Ed.* **2024**, *63*, 202405880.

[16] R. Cao, J. Chen, K. S. Han, W. Xu, D. Mei, P. Bhattacharya, M. H. Engelhard, K. T. Mueller, J. Liu, J.-G. Zhang, *Adv. Funct. Mater.* **2016**, *26*, 3059.

[17] a) Z. Guan, X. Chen, F. Chu, R. Deng, S. Wang, J. Liu, F. Wu, *Adv. Energy Mater.* **2023**, *13*, 2302850; b) Z.-X. Chen, Q. Cheng, X.-Y. Li, Z. Li, Y.-W. Song, F. Sun, M. Zhao, X.-Q. Zhang, B.-Q. Li, J.-Q. Huang, *J. Am. Chem. Soc.* **2023**, *145*, 16449; c) Y.-W. Song, L. Shen, N. Yao, S. Feng, Q. Cheng, J. Ma, X. Chen, B.-Q. Li, Q. Zhang, *Angew. Chem., Int. Ed.* **2024**, *63*, 202400343.

[18] M. M. Rahman, A. Ronne, N. Wang, Y. Du, E. Hu, *ACS Energy Lett.* **2024**, *9*, 2024.

[19] E. V. Karaseva, L. A. Khramtsova, A. N. Lobov, E. V. Kuzmina, D. Eroglu, V. S. Kolosnitsyn, *J. Power Sources* **2022**, *548*, 231980.

[20] Y. Lin, Y. Zhou, S. Huang, M. Xiao, D. Han, J. Qin, S. Wang, Y. Meng, *Adv. Energy Mater.* **2022**, *12*, 2201912.

[21] Y. Wang, Z. Wu, F. M. Azad, Y. Zhu, L. Wang, C. J. Hawker, A. K. Whittaker, M. Forsyth, C. Zhang, *Nat. Rev. Mater.* **2024**, *9*, 119.

[22] A. J. Bard, L. R. Faulkner, H. S. White, *Electrochemical methods: fundamentals and applications*, John Wiley & Sons, Hoboken, NJ, USA **2022**.

[23] a) H. Chu, H. Noh, Y.-J. Kim, S. Yuk, J.-H. Lee, J. Lee, H. Kwack, Y. Kim, D.-K. Yang, H.-T. Kim, *Nat. Commun.* **2019**, *10*, 188; b) M. Li, X. Huang, C. C. Su, K. Amine, *J. Am. Chem. Soc.* **2024**, *146*, 23182.

[24] a) H. Ji, Z. Wang, Y. Sun, Y. Zhou, S. Li, J. Zhou, T. Qian, C. Yan, *Adv. Mater.* **2023**, *35*, 2208590; b) Y.-W. Song, L. Shen, N. Yao, X.-Y. Li, C.-X. Bi, Z. Li, M.-Y. Zhou, X.-Q. Zhang, X. Chen, B.-Q. Li, J.-Q. Huang, Q. Zhang, *Chem* **2022**, *8*, 3031; c) F. Chu, M. Wang, J. Liu, Z. Guan, H. Yu, B. Liu, F. Wu, *Adv. Funct. Mater.* **2022**, *32*, 2205393.

[25] a) K. Xu, *J. Power Sources* **2023**, *559*, 232652; b) K. Xu, *Electrolytes, Interfaces and Interphases*, The Royal Society of Chemistry, Cambridge **2023**.

[26] a) D. Aurbach, E. Pollak, R. Elazari, G. Salitra, C. S. Kelley, J. Affinito, *J. Electrochem. Soc.* **2009**, *156*, A694; b) S. S. Zhang, *J. Power Sources* **2016**, *322*, 99.

[27] C.-X. Bi, N. Yao, X.-Y. Li, Q.-K. Zhang, X. Chen, X.-Q. Zhang, B.-Q. Li, J.-Q. Huang, *Adv. Mater.* **2024**, *36*, 2411197.

[28] D. Chai, Y. Zhu, C. Guan, T. Zhang, S. Tang, H. Zhu, X. Li, Y. Fu, *Energy Storage Mater.* **2023**, *62*, 102957.

[29] J. Li, J. Yang, Z. Ji, M. Su, H. Li, Y. Wu, X. Su, Z. Zhang, *Adv. Energy Mater.* **2023**, *13*, 2301422.

[30] G. M. Hobold, C. Wang, K. Steinberg, Y. Li, B. M. Gallant, *Nat. Energy* **2024**, *9*, 580.

[31] F. Wu, F. Chu, G. A. Ferrero, M. Sevilla, A. B. Fuertes, O. Borodin, Y. Yu, G. Yushin, *Nano Lett.* **2020**, *20*, 5391.

[32] Y. Liu, Y. Elias, J. Meng, D. Aurbach, R. Zou, D. Xia, Q. Pang, *Joule* **2021**, *5*, 2323.